The Meteoritical Society

Meteoritics & Planetary Science 1–13 (2024)
doi: 10.1111/maps.14253

Shock melt in the Cold Bokkeveld CM2 carbonaceous chondrite and the response of C-complex asteroids to hypervelocity impacts

Martin R. LEE[1]*, Luke DALY[1,2,3], Jennika GREER[1], Sammy GRIFFIN[1], Cameron J. FLOYD[1], Levi TEGG[2], and Julie CAIRNEY[2]

[1]School of Geographical and Earth Sciences, University of Glasgow, Glasgow, UK
[2]Australian Centre for Microscopy and Microanalysis, The University of Sydney, Sydney, New South Wales, Australia
[3]Department of Materials, University of Oxford, Oxford, UK

***Correspondence**
Martin R. Lee, School of Geographical and Earth Sciences, University of Glasgow, Glasgow G12 8QQ, UK.
Email: martin.lee@glasgow.ac.uk

(Received 02 March 2024; revision accepted 05 August 2024)

Abstract–Many of the CM carbonaceous chondrites are regolith breccias and so should have abundant evidence for collisional processing. The constituent clasts of these fragmental rocks frequently display compactional petrofabrics; yet, olivine microstructures show that most CMs are unshocked. To better understand the reasons for this contradiction, we have sought other evidence for hypervelocity impact processing of CM chondrites using the Cold Bokkeveld meteorite. We find that this regolith breccia contains rare particles of vesicular shock melt that are close in chemical composition to bulk CM chondrite. Transmission electron microscopy of a melt bead shows that it is composed of silicate glass with inclusions of pentlandite, pyrrhotite, and wüstite. Characterization of shards of another bead by atom probe tomography reveals nanoscale clusters of sulfur that represent sulfide inclusions arrested at an early stage of growth. These glass particles are mineralogically comparable to micrometeoroid impact melt described from the Cb-type asteroid Ryugu and melt that has been experimentally produced by pulsed laser irradiation of CM targets. The glass could have formed by in situ shock-melting, but petrographic evidence is more consistent with an origin as ballistic ejecta from a distal impact. The scarcity of melt in this meteorite, and CM chondrites more broadly, is consistent with the explosive fragmentation of hydrous asteroids following energetic collisions. Cold Bokkeveld's parent body is likely to be a second-generation asteroid that was constructed from the debris of one or more earlier bodies, and only a small proportion of the reaccreted material had been highly shocked and melted.

INTRODUCTION

The CM group of carbonaceous chondrites (CCs) are derived from one or more C-complex asteroids, and many of these meteorites are regolith breccias (Bischoff et al., 2006; Krietsch et al., 2021; Metzler et al., 1992). The clasts are typically sub-mm in size and have been partially or completely aqueously altered (i.e., C2 and C1 lithologies, respectively). These lithic fragments are supported in a fine-grained clastic matrix that contains solar-wind-implanted noble gases (Metzler et al., 1992), and hosts olivine grains with damage tracks produced by heavy ions from solar and galactic cosmic radiation (Goswami & Lal, 1979; Metzler, 2004). The track density of one clast in Cold Bokkeveld, a CM meteorite that is the focus of the present study, shows that it had spent at least 3 Myr in the outermost few meters of its parent body (Metzler, 2004).

Given their exposure to the space environment and abundance of lithic clasts, CM regolith breccias might be

expected to have ample evidence for impacts of both micrometeoroids and larger projectiles. Many of the CMs do indeed record collisions in the form of petrofabrics defined by the alignment of flattened objects including chondrules (Hanna et al., 2015; Lindgren et al., 2015; Rubin, 2012; Vacher et al., 2018; Yang et al., 2022). The shock pressures experienced by these meteorites can be quantified using olivine microstructures. Of the 25 CMs studied by Scott et al. (1992), 23 were unshocked (i.e., S1, <4–5 GPa shock pressure), one was classified as S1 and S2, and one S2 (5–10 GPa). They also noted that shock veins and melt pockets were absent. Rubin (2012) classified seven CMs and found all to be unshocked.

There are several possible explanations for why CM regolith breccias are typically unshocked. One is that impact energy was attenuated by the collapse of pores and brittle deformation of chondrules (e.g., microfracturing, grain boundary sliding; Hanna et al., 2015; Rubin, 2012). Lindgren et al. (2015) suggested that the contradiction between presence of petrofabrics and low shock stages can be reconciled by multiple low-energy impacts. Scott et al. (1992) attributed the lack of evidence for high energy impacts to explosive comminution and ejection of shocked and melted material promoted by the high porosity of CM lithologies and the presence of water ice. This hypothesis was supported by experiments in Tomeoka et al. (2003) showing that at pressures above 25 GPa hydrous and porous asteroids undergo comminution and melting, and the fine-grained material is lost to space. Suttle et al. (2017) concluded that low-energy impacts produced petrofabrics whereas higher shock pressures led to catastrophic disruption, with the debris potentially reaccreting into second-generation rubble pile asteroids.

Fresh insights into the nature of shock processing of C-complex asteroids have recently come from the discovery of particles of impact melt in three hydrous CCs: Nogoya (CM2), Diepenveen (CM2-an), and Orgueil (CI) (Langbroek et al., 2019; Zolensky et al., 2018, 2022). The presence of these objects suggests that impact melt could be more common than believed (i.e., it was not all lost to space by explosive fragmentation) and has either not been recognized as such or has been obscured by later physical/chemical alteration. We have sought to test these explanations by seeking impact melt in the Cold Bokkeveld CM2 chondrite. This meteorite was chosen because it is a breccia that is unshocked, yet some of its clasts have spent a considerable time in a regolith environment (Metzler, 2004; Metzler et al., 1992).

MATERIALS AND METHODS

Cold Bokkeveld was seen to fall in South Africa in 1838, and 5.2 kg was recovered (Graham et al., 1985). It is a gas-rich regolith breccia (Metzler et al., 1992) and has been heavily aqueously altered. The meteorite has been classified as petrologic type 1.3 (Alexander et al., 2013) and 1.4 (Howard et al., 2015), and subtype CM2.2 (Rubin et al., 2007) and CM2.1–2.7 (Lentfort et al., 2021). The range of subtypes in the latter classification reflects the petrologic diversity of the meteorite's abundant lithic clasts. Cold Bokkeveld has a shock stage of S1 (Rubin, 2012; Scott et al., 1992) and displays petrofabrics defined by flattened chondrules (Floyd et al., 2023; Lindgren et al., 2015; Rubin, 2012; Suttle et al., 2017; Zolensky et al., 1997).

Several polished blocks of Cold Bokkeveld loaned by the Natural History Museum, London, were initially studied. Impact-formed glass was found in only one block, BM1727 P19256, which is the focus of the present study (hereafter "P19256"). This sample is roughly rectangular in shape and 10.6 by 5 mm in size (Figure 1). After coating with ~10 nm of carbon, it was characterized by backscattered electron (BSE) imaging using a Zeiss Sigma field-emission scanning electron microscope (SEM) operated at 20 kV/~1 nA at the University of Glasgow (UoG) (Figure 1). X-ray maps and spot analyses were acquired using the same SEM equipped with an Oxford Instruments 150 mm^2 X-Max energy-dispersive X-ray spectrometer (EDS) operated through Oxford Instruments AZtec software. For quantitative chemical analysis, the Sigma SEM was operated at 20 kV/2 nA in spot mode, with a count time of 60 s. Calibration used the following standards: Na (jadeite) Mg (periclase), Al (garnet), Si (olivine), P (apatite), S (pyrite), Ca (wollastonite), Ti (rutile), Cr (chromite), Mn (rhodonite), Fe (garnet), and Ni (Ni metal). Approximate detection limits were 0.1 wt% element, and the analytical precision for elements close to detection limits was $\pm \sim 5\%$ as determined by repeat analysis of standards.

An electron-transparent wafer was cut from a particle of glass for characterization by transmission electron microscopy (TEM) and transmission Kikuchi diffraction (TKD) at the UoG. The wafer was prepared from the polished block using a FEI Helios plasma-focused ion beam (FIB) microscope operated at 30 kV. Following extraction using an in situ micromanipulator, the wafer was welded to a copper support grid using electron- and ion-deposited platinum, then loaded into a double-tilt goniometer holder. Bright-field TEM images and selected area electron diffraction (SAED) patterns were acquired from the wafer using a FEI T20 TEM operated at 200 kV. The d-spacings of SAED patterns were calibrated using FIB-deposited platinum. For TKD work, the wafer was mounted on a pre-tilted holder and studied using the Zeiss Sigma SEM operated at 20 kV. Forescatter electron images and

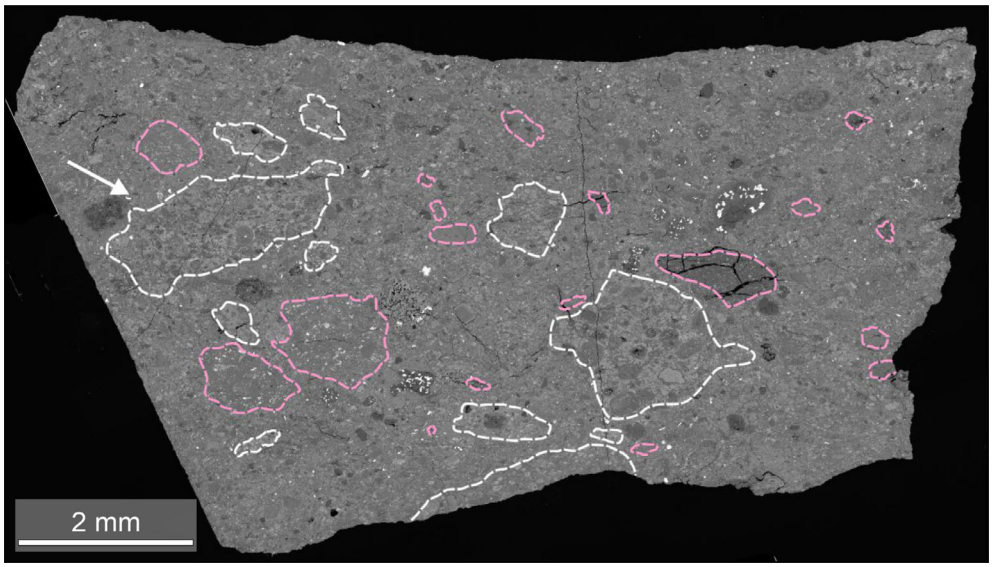

FIGURE 1. BSE image of Cold Bokkeveld P19256. Areas of primary accretionary rock are outlined in white, and clasts of other C2 and C1 lithologies in pink. The location of the glass bead is indicated by the white arrow (upper left).

electron backscatter diffraction patterns were acquired using Oxford Instruments Symmetry 2 electron backscatter diffraction (EBSD) system.

Samples for atom probe tomography (APT) were prepared at the University of Sydney (USyd) using a Thermofisher G4 Hydra Plasma FIB-SEM. A lamella was cut and lifted out from several glass particles. During the final stages of tip sharpening the sample was cooled to 70 K using a cryo-stage within the SEM and transferred to the atom probe using a transfer shuttle under cryogenic and vacuum conditions (Cairney et al., 2019). Five nanotips were analyzed using a LEAP 4000X Si at USyd, and useable data sets were obtained from two of them. APT data acquisition settings were $T = 50$ K, a detection rate of 0.3%, a pulse rate of 250 kHz, and a pulse energy of 40 pJ. Reconstruction of the APT data used CAMECA's AP Suite 6.

RESULTS

Petrography of Polished Block P19256

We first describe the sample's constituent lithologies, then the evidence for impact melt. The polished block comprises two lithologies that are petrographically comparable to "primary accretionary rock" and "fine grained clastic matrix" (hereafter "clastic matrix") of Metzler et al. (1992) (Figures 1 and 2a). Areas of primary accretionary rock are surrounded by clastic matrix, with sharp contacts between the two (Figure 2a). Primary accretionary rock contains chondrules, calcium- and aluminum-rich inclusions (CAIs), and coarse mineral grains, most of which have fine-grained rims (Figure 2a). These objects are set in a fine-grained phyllosilicate-rich matrix containing tochilinite–cronstedtite intergrowths (TCIs) and Ca-carbonate grains. Some areas of primary accretionary rock have a petrofabric that is defined by flattened and aligned TCIs and chondrules (Figure 2b). The clastic matrix also contains rimmed chondrules, CAIs, and coarse mineral grains, but differs from primary accretionary rock in that TCIs are less abundant, and C2 and C1 clasts are present (Figures 1 and 2d). The petrologic (sub)types of the primary accretionary rock and clastic matrix lithologies have not been determined, but their mineralogy and petrographic properties are consistent with the host meteorite's petrologic classifications (i.e., type 1.3–1.4, subtype ~CM2.2).

Glass Particles

Petrographic Properties

The clastic matrix contains a circular object 15 μm in diameter that is hereafter referred to as the glass bead (Figures 1, 2c, and 3). Adjacent to it are angular pieces of a petrographically comparable material that are described as the shards (Figure 3a–c). The bead and shards are vesicular and contain inclusions up to 800 nm diameter that are identified as Fe-Ni sulfide by SEM-EDS (Figure 3b,c and Figure S1). The glass particles have sharp contacts with the enclosing clastic matrix, and the left-hand side of the bead has been fractured leading to slight rotation of resulting fragments (Figure 3b,c). The shards have the appearance of fragments of a bead, and it is notable that they are aligned along one side of a TCI (Figure 3b).

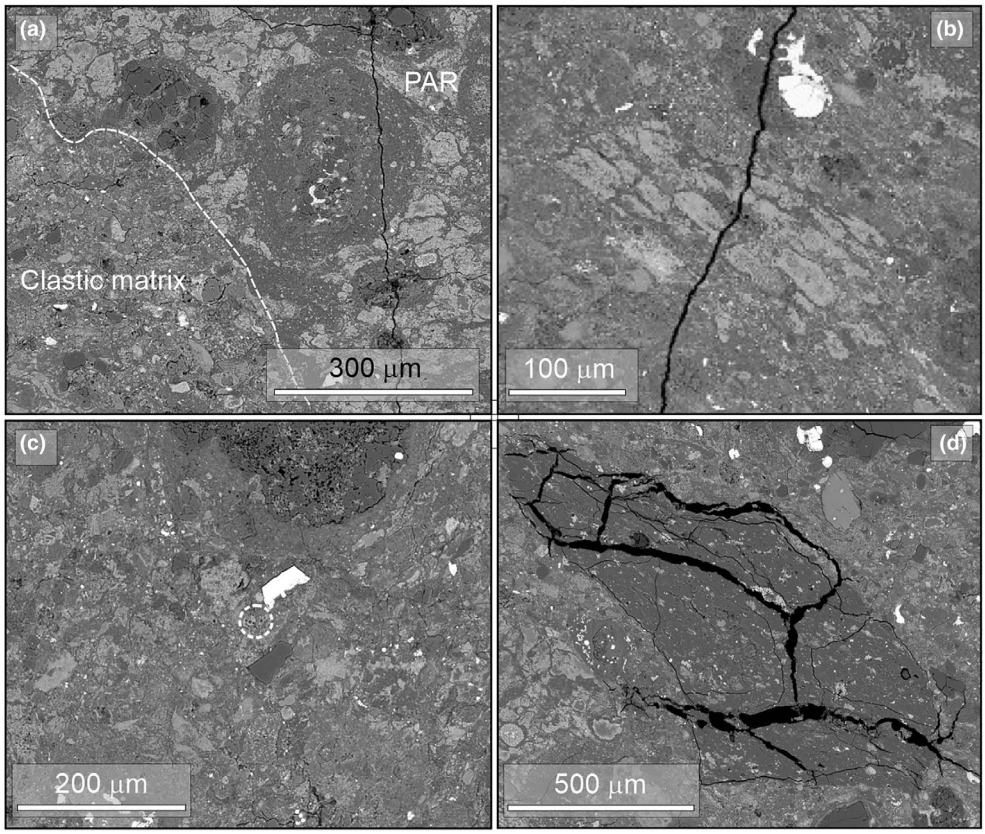

FIGURE 2. BSE images of Cold Bokkeveld P19256. (a) The contact between primary accretionary rock (PAR) and clastic matrix is delineated by a dashed white line. The PAR contains an intact chondrule with a fine-grained rim, and to the left of it is another rimmed chondrule that is cut by the clastic matrix. (b) A clast of PAR containing abundant flattened TCIs that are oriented with their long axes SE-NW in the image. (c) An area of clastic matrix containing the glass particles, which are in the middle of the image and outlined by a white circle. Other constituents of this lithology include a sulfide crystal (white), TCIs (light gray), and a rimmed chondrule (top of the image). (d) A C1 clast that is fractured in contrast to the enclosing clastic matrix.

Chemical Composition

The bead has a Mg-Fe silicate composition with 2.6–4.1 wt% Al_2O_3, 1.7–2.6 wt% S, 1.7–2.5 wt% CaO, and 1.0–1.9 wt% NiO, and analytical totals close to 100 wt% (Table 1). The elemental composition of the bead is compared to bulk CM and CI chondrites in Figure 4a. Also plotted are analyses of CM chondrite melt from two other contexts: Cold Bokkeveld fusion crust (Figure 4a), and melt produced in shock-recovery experiments on Murchison (CM2) (Figure 4b,c). The bead is close to bulk CM chondrite in most of the plotted elements. The main differences are enrichment of the bead in Al, the most refractory element, and to a lesser extent Fe, and depletion in Ni, Cr, and especially the most volatile element S. In contrast, the bead differs significantly from bulk CI values in the three most refractory elements. Cold Bokkeveld fusion crust shows a similar pattern to the bead, although it is more depleted relative to bulk CM chondrite in Ni, depleted instead of enriched in Fe, and more highly depleted than the bead in S. The shock melt is highly depleted and enriched in many elements relative to bulk CM values (Figure 4b,c).

Mineralogy

The bead is composed of an Mg-Fe silicate glass, which produces a characteristic broad ring in SAED patterns (Figures 5 and 6). The glass has abundant inclusions, most of which are sulfides, and they have a bimodal size distribution (~1–2 μm and ~20–200 nm) (Figures 5e and 6a–c). The largest inclusions are close to the bead's outer edge, and the smaller ones occur throughout its interior (Figure 5e). SAED patterns of most inclusions index as pentlandite, although two of the larger ones are pyrrhotite. Both pyrrhotite inclusions are distinctive in having tendrils that extend into the enclosing glass (Figure 6c). At one side of the bead (the left-hand edge in Figures 5 and 6) is a ~400 nm wide band within which inclusions are very abundant and

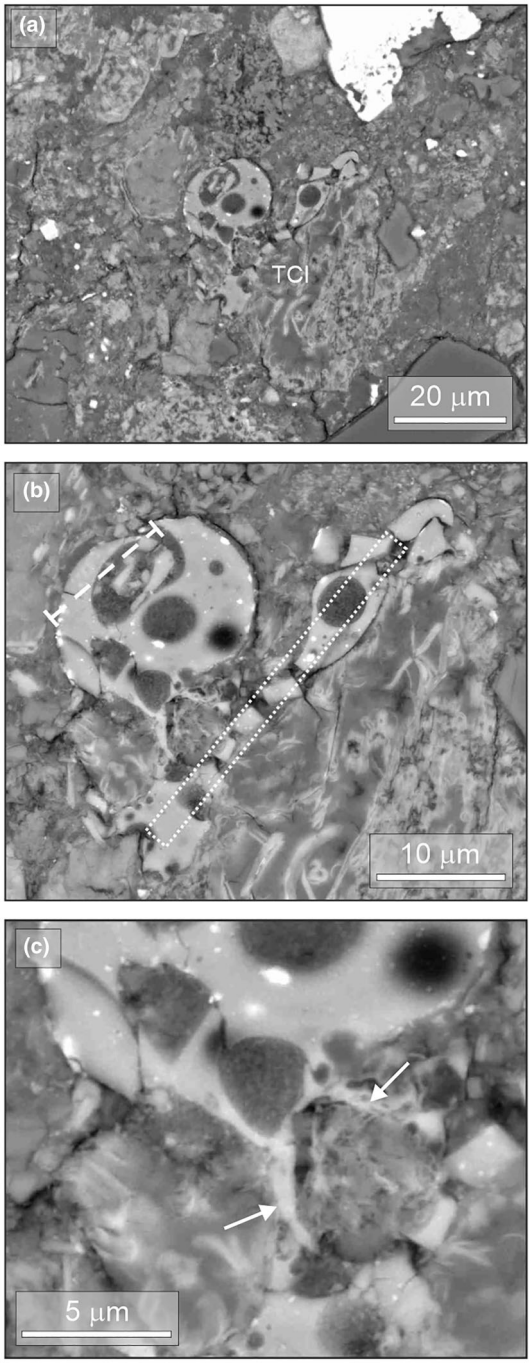

FIGURE 3. BSE images of the glass particles. (a) The bead is in the middle of the image, with shards to its right-hand side. The shards are aligned along the left-hand edge of an area of TCI (labeled). (b) The bead and shards. They have the same mid-gray contrast, indicating a comparable mean atomic number. They also contain vesicles together with small white grains of Fe-Ni sulfide. The dashed white line in the bead delineates the midplane of a FIB wafer that was extracted from it, and the white rectangle shows where APT tips were removed from the shards. EDS element maps of this field of view are in Figure S1. (c) Part of the bead and adjacent shards. The left-hand edge of the bead has been fractured and in the lower right-hand side are two curved selvages (arrowed) that may outline part of a ruptured vesicle.

uniformly small (~20 nm in diameter) (Figure 6d). SAED patterns obtained from the band have rings with d-spacings of ~0.25, 0.21, and 0.15 nm in addition to the broad diffraction ring from host glass. These d-spacings are consistent with both periclase (MgO) and wüstite (FeO), but the two minerals cannot be distinguished within the precision of this SAED technique. As the band has a higher Fe/Mg ratio than the interior of the bead (Figure 5c,g), its inclusions are more likely to be wüstite or a mineral toward the Fe end of the solid solution (e.g., magnesiowüstite). The clastic matrix enclosing the bead contains angular grains of enstatite and diopside, and Mg-rich phyllosilicates that SAED shows are crystalline (Figures 5 and 6).

Nanoscale Chemistry from Atom Probe Tomography

Atom probe reconstructions of two of the tips extracted from the shards reveal clusters of S (peak at 64 Da) that do not spatially correlate with clusters of Fe, Mg, or O (peak series at 12, 16, 24, 28, 32, 56, and 72 Da) (Figure 7a,b). In one of the tips nanoscale S features are present within a larger S cluster (Figure 7b). These clusters additionally contain other major (Si) and minor (Al) elements that are also present in the host glass and so could reflect the intrinsic chemistry of the clusters or fuzziness in spatial resolution of the technique. Mass spectra corresponding to these tips are in Figure S2.

DISCUSSION

We start by appraising how the Cold Bokkeveld breccia was assembled and lithified, then evaluate the origin of the glass particles with the help of comparisons with melt previously described from laser irradiation experiments, asteroid Ryugu, and CC meteorites. We finish by considering the insights that Cold Bokkeveld glass offers into the origin and history of CM regolith breccias, and the response of hydrous asteroids to hypervelocity impacts.

Construction and Lithification of the Cold Bokkeveld Breccia

The sample studied is consistent with a CM regolith breccia comprising clasts (primary accretionary rock, other C2 lithologies, and C1 lithologies) in a clastic matrix. The primary accretionary rock clasts are likely to be locally derived (Metzler et al., 1992) whereas the source of the other lithic clasts is hard to determine; they could be from the primary accretionary rock's parent body, or from a different asteroid (i.e., xenoliths). Irrespective of their provenance, the petrologic variety of the clasts is consistent with the breccia being assembled after they had been aqueous altered (e.g., Lindgren

TABLE 1. Chemical composition of the bead (wt%).

	Analysis 1	Analysis 2	Analysis 3	Analysis 4	Analysis 5	Analysis 6
SiO_2	32.1	31.2	32.0	31.5	32.0	33.2
Al_2O_3	3.2	4.1	3.6	2.6	3.2	3.1
Cr_2O_3	0.5	0.5	0.5	0.5	0.5	0.5
FeO	36.1	35.5	35.1	35.1	36.8	36.1
MnO	0.3	0.3	0.3	0.2	0.2	0.3
MgO	21.1	20.9	21.1	21.4	21.2	22.0
CaO	1.9	1.8	2.0	2.5	1.7	1.8
Na_2O	0.7	0.7	0.7	0.7	0.7	0.7
P_2O_5	d.l.	0.3	0.3	d.l.	0.3	d.l.
NiO	1.7	1.4	1.0	1.6	1.9	1.7
S	2.2	1.8	1.7	2.5	2.6	2.2
Total	99.6	98.4	98.1	98.5	101.0	101.5

Abbreviation: d.l., below detection limits.

et al., 2013). The C1 and C2 lithologies must, therefore, have come from depth (i.e., from regions within a body where temperatures and pressures were sufficiently high to support water/rock interaction for an extended period). They could have been excavated by impacts or by explosive fragmentation following the internal accumulation of gases generated by aqueous alteration (Wilson et al., 1999), and both processes would have led to considerable disruption of the body.

Some of the primary accretionary rock clasts have petrofabrics defined by the common alignment of flattened chondrules and TCIs (Figure 2b). Such textures have been previously described by Cold Bokkeveld (Greenwood et al., 1994; Rubin, 2012; Suttle et al., 2017) and other CM chondrites (Hanna et al., 2015; Lindgren et al., 2015; Rubin, 2012; Yang et al., 2022). In all cases, the petrofabrics are interpreted to have formed by impact compaction, and the shock-recovery experiments of Tomeoka et al. (1999) indicate that chondrule flattening requires minimum pressures of ~4–10 GPa. With regard to P19256, the clasts must have been deformed before being juxtaposed because not all of them have a petrofabric. The maximum shock pressures experienced by the clasts can be constrained by the lack of petrographic evidence for post-hydration heating (e.g., dehydration fractures). Such heating would require a minimum of ~11 GPa, which is the pressure at which samples of Murchison (CM2) underwent incipient devolatilization in an experimental study by Tyburczy et al. (1986). Thus, a proportion of the lithic clasts in P19256 were exposed to pressures sufficient to produce petrofabrics without heating (i.e., ~4–11 GPa), whereas others bear no evidence for dynamic compaction.

The most likely agent of lithification of the Cold Bokkeveld breccia was compaction by further impacts, and evidence for that process was provided by Floyd et al. (2023). They found that several C2 clasts in a different piece of the same meteorite have petrofabrics with a common orientation indicating that their constituent chondrules had been flattened and aligned after the clasts had been juxtaposed. However, the intensity of this late-stage compaction and concomitant lithification must have differed across Cold Bokkeveld's parent body because clasts in P19256 do not show a common petrofabric alignment.

Origin of the Cold Bokkeveld Glass Particles

Relative Timing of Incorporation into the Clastic Matrix

The glass particles are superficially similar to fusion crust. However, they did not form by frictional melting during the meteorite's atmospheric entry because they are not fragments of a melt layer, lack the characteristic magnetite and zoned olivine (Genge & Grady, 1999), and differ from fusion crust in chemical composition (Figure 4a). The bead and shards cannot have been present within Cold Bokkeveld prior to aqueous alteration because glass is very vulnerable to water/rock interaction and even at the TEM scale there is no evidence for its corrosion or replacement (Figures 5 and 6). However, as the bead has been fractured, and the shards were probably produced by breakage of another bead, they must have been present prior to compaction of the breccia. It is unclear why the shards are aligned along the edge of a patch of TCI (Figure 3a,b), but one possibility is that their precursor bead was broken up by a shear plane along which the shards were then spread.

Experimental Analogs

Melt particles produced by pulse laser irradiation of Murchison (Matsuoka et al., 2015, 2020; Thompson et al., 2019) are good analogs for the Cold Bokkeveld glass particles. The experiments of Matsuoka et al. (2015, 2020) generated S- and Fe-rich melt in the form of

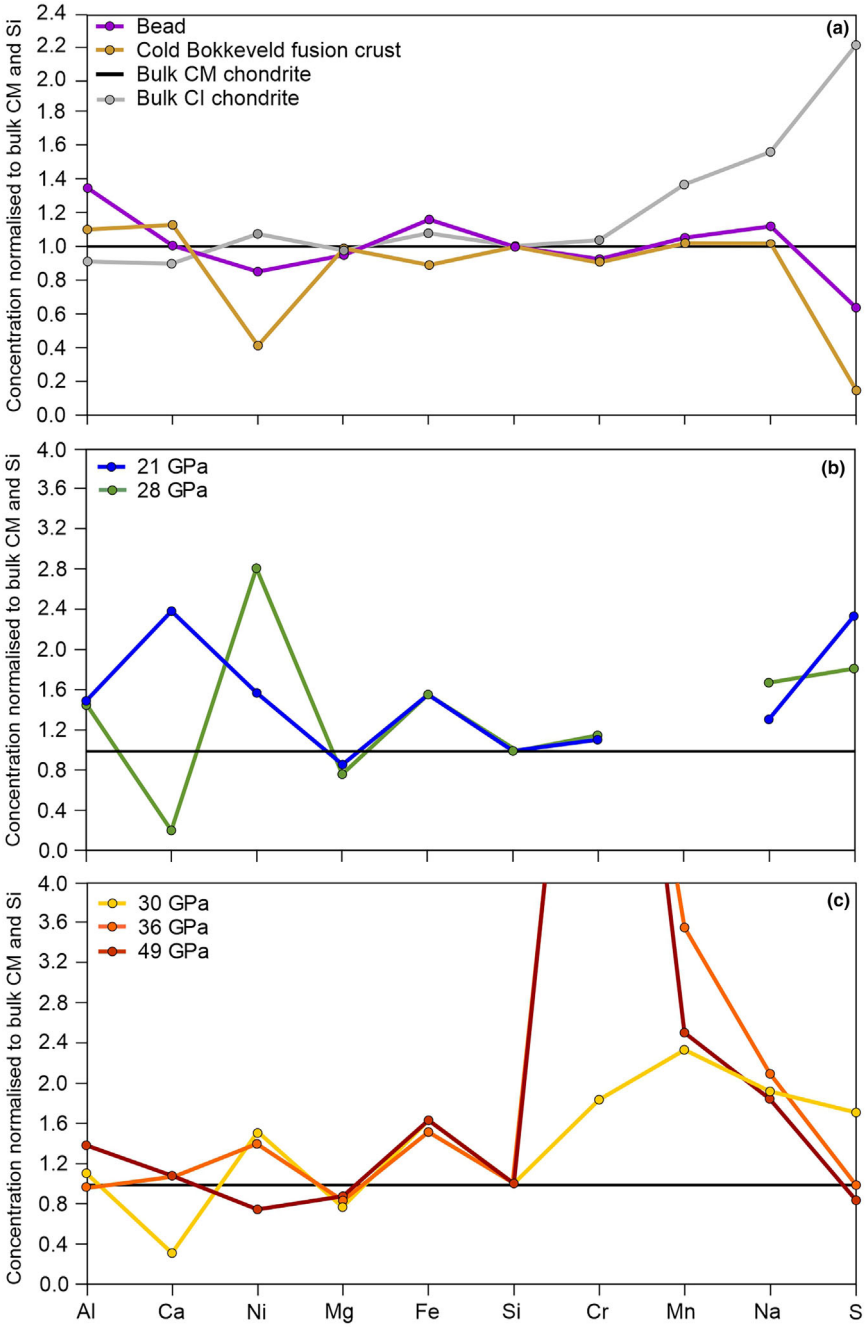

FIGURE 4. Elemental compositions of CM chondrite melts. Data are normalized to bulk CM CC (solid black line; values from Lodders, 2021) and Si. Elements are arranged from left to right in order of decreasing 50% condensation temperature (Lodders, 2003). (a) Average of six analyses of the Cold Bokkeveld bead, average of 16 analyses of Cold Bokkeveld fusion crust (data from Genge & Grady, 1999), and bulk CI chondrite (Lodders, 2021). The data plotted are listed in Table S1. (b) Impact melt produced in shock-recovery experiments on Murchison (CM2) at peak pressures of 21 and 28 GPa (Mn was below detection limits). (c) Impact melt produced in shock-recovery experiments on Murchison at peak pressures of 30, 36, and 49 GPa. Not shown are values for Cr from the 36 and 49 GPa experiments (8.97 and 9.39, respectively). Note the difference in *Y*-axis scale between (a), and (b) and (c).

globular structures and splash layers. These particles are up to ~1 μm in size, amorphous, vesicular, and contain pentlandite. Matsuoka et al. (2015) suggested that the melt was preferentially produced from tochilinite in the target owing to the hydrous sulfide's relatively low melting temperature. Thompson et al. (2019) collected

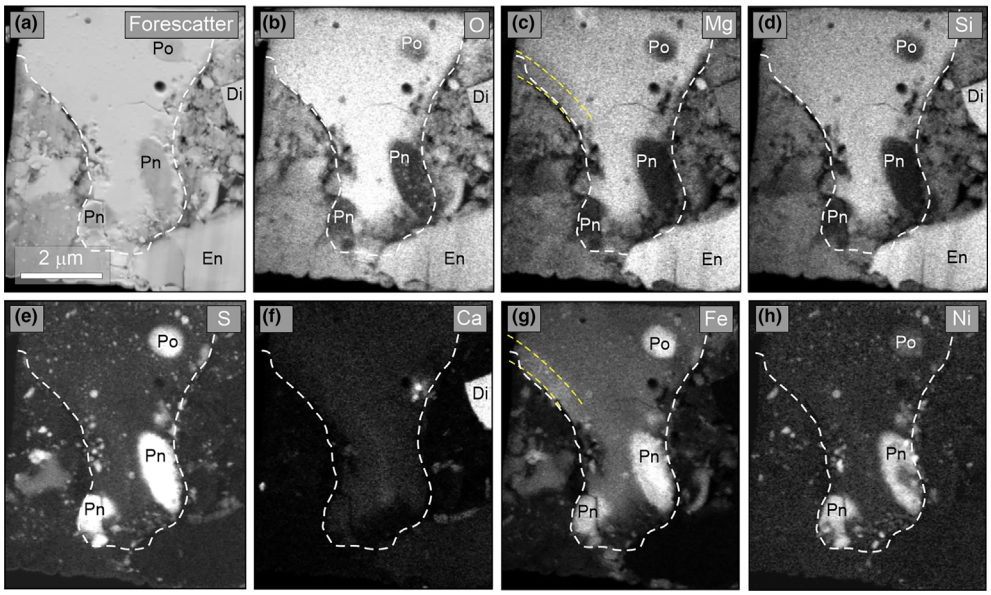

FIGURE 5. Forescatter electron image (a) and EDS element maps (b–h) of part of the FIB wafer that has sampled a region of the bead between its outer surface and the outer wall of a vesicle (see Figure 3b for the location of the wafer). There are two relatively large inclusions of pentlandite (Pn) and an inclusion of pyrrhotite (Po). Smaller sulfide inclusions that occur throughout the glass are located by white spots in (e). On the left-hand edge of the bead is a band that is depleted in Mg and enriched in Fe relative to its interior, as delineated by dashed yellow lines in (c) and (g). The clastic matrix contains angular grains of enstatite (En), diopside (Di), and finely crystalline phyllosilicates.

pancake- and dumbbell-shape melt deposits up to 250 nm in thickness that had been ejected from a Murchison sample during irradiation. The melt is vesicular, rich in Mg, Si, and Fe, and has inclusions up to 30 nm in size that are dominated by Fe-Ni sulfides (troilite, pentlandite) and magnetite. Spherules and droplets of vesicular melt up to 500 nm thick also formed on the outer surface of irradiated meteorite matrix. The melt has a Mg,Fe silicate composition with Fe-Ni sulfide nanoparticles up to 100 nm in size, the largest of which is pentlandite.

Comparison with Space Weathering of Ryugu

The Cold Bokkeveld glass particles are also similar in mineralogy and texture to products of space weathering of the Cb-type asteroid Ryugu that were returned by the Hayabusa2 mission. Noguchi et al. (2023) described "melt splashes" (<10 μm across) on ~1% of the grains from the two touchdown sites and "frothy layers" on 1%–2% of returned grains. The melt splashes are probable ejecta from micrometeoroid cratering. The frothy layers comprise silicate glass with ~0.1- to 1-μm-diameter vesicles and ubiquitous <10- to 200-nm diameter inclusions of pyrrhotite and pentlandite. The sulfides are interpreted to have formed by immiscible separation from silicate melt, although some of the ~10 nm size particles could be vapor deposited (Noguchi et al., 2023). Neither periclase nor wüstite were described from the frothy layer, but ferropericlase was identified in the space-weathered rim of a Ryugu breunnerite grain (Matsumoto et al., 2024). Apart from the micrometeoroid impact melt, there is no evidence for high-pressure shock metamorphism of Ryugu, and the returned samples experienced an average peak pressure of ~2 GPa (Tomioka et al., 2023). Whilst the Cold Bokkeveld glass particles are similar to the products of space weathering of Ryugu, the intact bead is larger than the Ryugu melt splashes and it has bigger vesicles, which could have formed by coalescence of smaller vesicles during relatively slow cooling.

Shock Melt in Other CCs

The Cold Bokkeveld glass particles are not unique to hydrous CC meteorites because glass-rich "agglutinates" have been described from Nogoya (CM2), Diepenveen (CM2-an), and Orgueil (CI1) (Langbroek et al., 2019; Zolensky et al., 2022). A 6-μm-diameter glassy spherule has also been recorded in Orgueil (Zolensky et al., 2018). The agglutinates have some similarities to the Cold Bokkeveld particles but also important differences. They all contain glass, which in Diepenveen and Orgueil hosts inclusions of Fe-Ni sulfide. At ~100–150 μm in size, the agglutinates are considerably larger than the Cold Bokkeveld bead and also differ in containing small euhedral olivine crystals that have formed by devitrification. The Nogoya and Diepenveen agglutinates

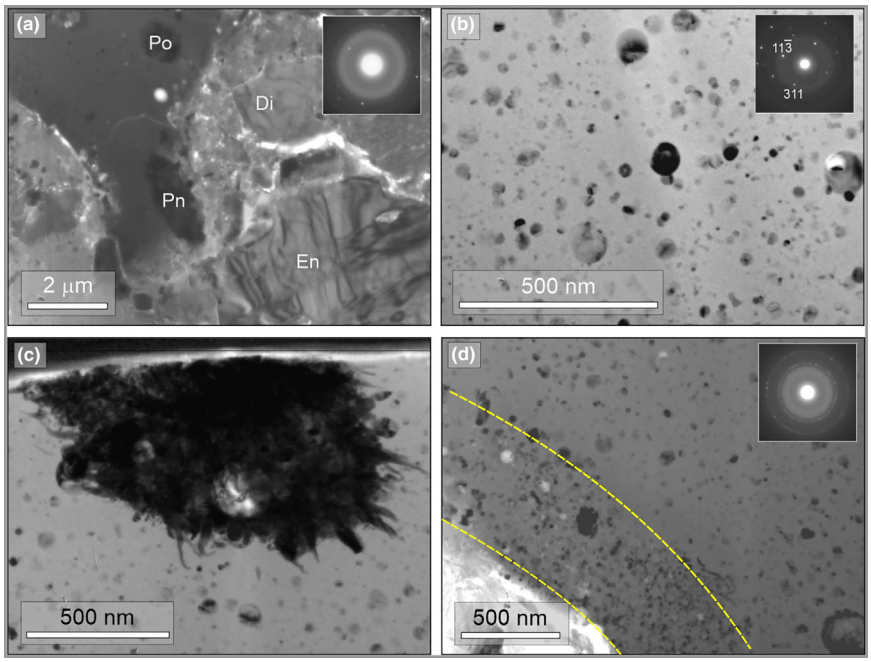

FIGURE 6. Bright-field TEM images and SAED patterns of part of the FIB wafer extracted from the bead. (a) The bead is on the left-hand side of the image and contains several micrometer size sulfide inclusions (black), identified by EDS and SAED as pentlandite (Pn) and pyrrhotite (Po). The inset SAED pattern is from the interior of the bead and its broad ring shows that it is predominantly glass. The enclosing clastic matrix contains grains of enstatite (En) and diopside (Di). (b) Interior of the bead comprising glass with abundant inclusions. The inclusion in the center of the image is 80 nm in diameter and its SAED pattern (inset) indexes as $[\bar{2}51]$ pentlandite. (c) An inclusion of pyrrhotite (black) with tendrils extending into the enclosing nanoparticle-rich glass. The black strip along the top of the image is FIB-deposited platinum. (d) A ~400 nm wide band at one edge of the bead (delineated by dashed yellow lines) within which nanoparticles are notably abundant. The inset SAED pattern was obtained from this band, and in addition to the broad diffraction ring from the glass, it has rings with d-spacings of ~0.25, 0.21, and 0.15 nm that are consistent with periclase (MgO) and wüstite (FeO).

are further distinct in hosting un-melted silicate and sulfide grains (olivine, low-Ca pyroxene, troilite), and phyllosilicates surrounding the Orgueil and Nogoya agglutinates has been thermally altered (Zolensky et al., 2022). These properties are consistent with the agglutinates having been produced by in situ impact melting of hydrous regolith, and the chemical compositions of those in Orgueil and Nogoya suggest that they were formed from CI1 and CM2 lithologies, respectively (Zolensky et al., 2022). Despite hosting impact melt, Nogoya is unshocked (S1; Scott et al., 1992) whereas the shock stages of Diepenveen and Orgueil have not been determined. A ~1 mm size object made of zoned olivine microphenocrysts in glass that occurs in the regolithic howardite Grosvenor Mountains (GRO) 95574 is also interpreted to have formed by impact melting of a CM lithology (Lunning et al., 2016). In this case, the melt was ejected from the target as a droplet and was eventually accreted by the howardite parent body.

Origin of Cold Bokkeveld Shock Melt

Comparisons with the products of pulsed laser irradiation of Murchison, Ryugu grains, and CC agglutinates indicate that the Cold Bokkeveld glass particles formed by shock melting of a CC lithology. The bead's chemical composition and presence of vesicles indicate an origin from melting of a target with a hydrous Mg-Al-Si-S-Fe composition (i.e., a fine-grained CM lithology rather than an individual silicate or sulfide mineral grain). There was little fractionation relative to bulk CM composition with regard to the majority of elements plotted in Figure 4a, although the most volatile element, S, is significantly depleted and the most refractory, Al, is enriched. Cold Bokkeveld fusion crust shows a greater fractionation of Ni and Fe relative to bulk CM than the bead, which is likely due to the loss of Fe-Ni sulfide liquids and further depletion of S through degassing (Genge & Grady, 1999). The Murchison shock melt shows quite different compositional profiles to the bead (Figure 4), which could reflect the nature of element fractionation during in situ shock melting, but is more likely to be due to the presence of inclusions of un-melted target rock.

The abundance of glass in the bead shows that the melt cooled rapidly. The nanoscale inclusions of pentlandite and pyrrhotite could have formed following

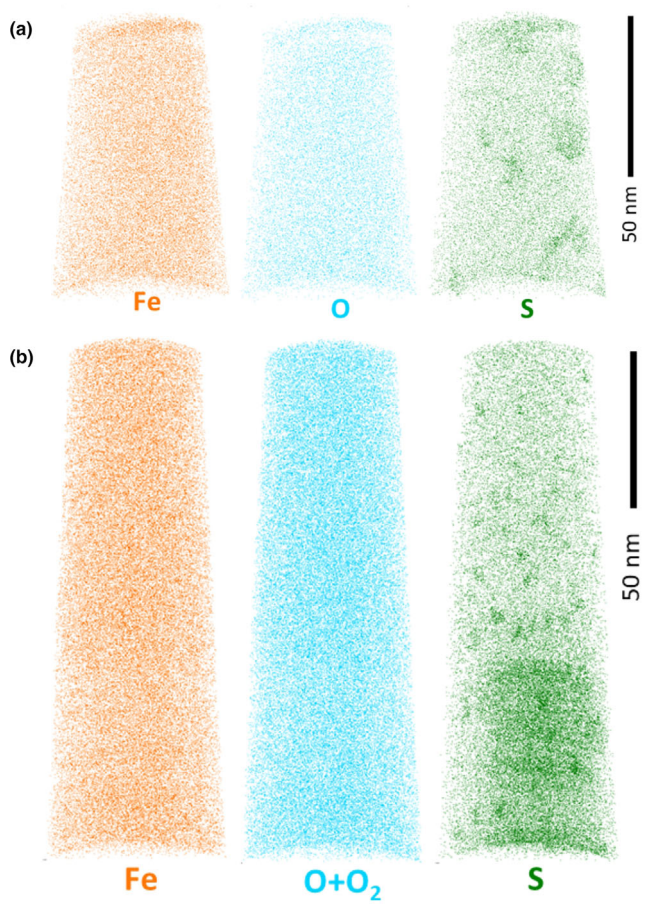

FIGURE 7. (a) Reconstruction of tip M22 with Fe (orange) O (blue) and S (green) atoms plotted; the latter highlights nanoscale features that are irregular in shape. Ni (not shown) has a slight correlation with S. (b) Reconstruction of M14 with Fe (orange), O (blue), and S (green) atoms plotted. An increase in S at the base of the tip is also associated with a more variable H and increased minor element concentration. The S clusters do not spatially correlate with elevated abundances of Ni or any other element.

the immiscible separation of the Fe-Mg silicate and sulfide components of the melt. Alternatively, given that the solubility of sulfur in mafic melts positively correlates with temperature (Haughton et al., 1974; Yang, 2012), the inclusions may have formed as sulfur solubility decreased during cooling of the melt. The APT tips show nanoscale clusters of sulfur rather than Fe(Ni) sulfide nanoparticles. One explanation for this unexpected finding is that the shards from which the APT tips were made lacked inclusions, although sulfides were identifiable by SEM (Figure 3b,c). Another possible reason for the absence of Fe(Ni) sulfides in APT tips could be that the presence of nanoparticles means that they do not run well during APT analysis such that the only useable data sets were from glass-rich and sulfide-poor tips. Our favored explanation is that the clusters formed by sulfur came out of the melt as it cooled (owing to its solubility decreasing with falling temperature as noted above), and there was not enough time for sulfide nanoparticles to grow.

Shock-recovery experiments using Murchison (Tomeoka et al., 1999, 2003) can help estimate the impact energy needed to melt a Cold Bokkeveld lithology. They found that local melting occurs at 20–30 GPa due to frictional heating along fractures (analogous to pseudotachylites), is more pervasive at >35 GPa, and complete at >49 GPa. The melt is vesicular, contains spherules of Fe-Ni metal and Fe-sulfide, and forms veins and pockets. Relative to unshocked matrix, the melt is commonly enriched in Fe, S, and often Ca reflecting the contributions of Fe, Ni metal, tochilinite, Fe-sulfide, Fe-rich serpentine, and calcite, with the vesicles being produced by devolatilization of the latter two minerals (Tomeoka et al., 1999). Although the pressure thresholds for melting cannot necessarily be directly applied to asteroid regoliths given the design of the shock-recovery experiments (samples ~0.5–1 cm diameter in ~2 × 3 cm size steel holders; Tomeoka et al., 1999), the melt particles in Cold Bokkeveld, and agglutinates in other CCs, are indicative of shock pressures in excess of ~20 GPa (i.e., shock stage >S3).

The glass particles could have been produced by in situ melting, or may have been added to the Cold Bokkeveld breccia after having been transported from one or more distal impact sites (i.e., an "ex-situ" origin). An argument in favor of in situ melting is the occurrence of two melt particles next to each other (one of which has been broken into shards). Such co-location is understandable if the melt had formed in place, but quite a coincidence if the particles had been transported from elsewhere, especially given the scarcity of glass in the polished block. However, we favor an ex situ origin for the glass particles for several reasons: (i) the shape of the bead (i.e., akin to a melt droplet); (ii) absence from the bead of inclusions of un-melted target rock—such inclusions characterize the Nogoya and Diepenveen agglutinates, and may also be responsible for the compositional differences between Murchison shock melt and bulk CM chondrite (Figure 4b,c); (iii) the lack of evidence for thermal alteration of fine-grained phyllosilicates within a few micrometers of the bead (i.e., TEM shows that they are crystalline), thus demonstrating that it had cooled when juxtaposed with the hydrous matrix of Cold Bokkeveld. In addition, the Cold Bokkeveld meteorite does not have microstructural evidence for the >~20 GPa of shock pressure needed for in situ melting. Thus, the Cold Bokkeveld glass particles are interpreted to be ballistic ejecta from one or more distal impacts, with the melt cooling and solidifying in flight.

Construction of CM Chondrite Breccias from Material with Diverse Shock Histories

As Cold Bokkeveld is a polymict breccia, it must have been built using lithologies sourced from different regions of the same body, or from two or more C-complex asteroids. The glass particles show that some of the breccia's constituents had been highly shocked. This interpretation is consistent with the evidence for construction of other CM breccias from both shocked and un-shocked material. For example, Scott et al. (1992) reported that 10%–20% of Murchison chondrules and chondrule fragments had been shocked prior to their juxtaposition with other olivine-bearing constituents of the meteorite, and Nogoya is unshocked despite containing an agglutinate particle.

A model for the mixing of CM lithologies with diverse shock histories was developed by Yang et al. (2022) using observations of Aguas Zarcas (CM2). They suggested that shocked material can move between different parts of C-complex asteroids by "pebble transport," as is currently taking place on the asteroid Bennu (Lauretta et al., 2019). Pebble transport may be initiated by impacts, or by other regolith processes such as dehydration of phyllosilicates and thermal fracturing. Although objects as small as the Cold Bokkeveld bead would not have been observable by the OSIRIS-REx spacecraft (Lauretta et al., 2019), it is likely that the pebble transport mechanism is also applicable to tens of micrometer size particles. An alternative explanation for mixing of variably shocked materials is that Cold Bokkeveld was derived from a second-generation rubble pile asteroid that had been built from the debris of one or more first-generation asteroids which had been fragmented by impacts. Some of the collisions were sufficiently energetic for local melting. This model is consistent with the conclusions of Scott et al. (1992) and Tomeoka et al. (2003) that hydrous asteroids respond to hypervelocity impacts by explosive disintegration, and with discovery of a xenolith of CM impact melt in GRO 95574 (Lunning et al., 2016). The second-generation parent body model is probably equally applicable to many other CM regolith breccias.

CONCLUSIONS

Cold Bokkeveld contains rare particles of glass that formed by shock melting of a CM chondrite lithology. This melting could have taken place in situ, but the lack of evidence for thermal alteration of phyllosilicates surrounding the glass particles or high-energy impact processing of the host meteorite indicates that they came from another region of Cold Bokkeveld's parent body, or from another C-complex asteroid. The shock melting could have been due to the impact of micrometeoroids (i.e., space weathering) or larger projectiles. In the former scenario, "pebble transport" might have been responsible for moving glass particles between different parts of Cold Bokkeveld's parent body, with them being incorporated into the breccia during regolith gardening. The scarcity of glass in Cold Bokkeveld, and other CM meteorites, suggests that space weathering is less likely an origin for the glass particles than shock melting accompanying a higher energy impact. Such a collision is likely to have fragmented the hydrous target asteroid, and the debris contributed to make Cold Bokkeveld's second-generation rubble pile parent body. In this scenario, most of the highly shocked fragments of the first-generation asteroid were lost to space and only a small proportion was reaccreted, thus accounting for the scarcity of glass in the meteorite.

Acknowledgments—We are grateful to the Natural History Museum London for the loan of the Cold Bokkeveld sample. The authors thank University of Glasgow staff Billy Smith and Colin How (School of Physics and Astronomy) for assistance with the FIB and TEM work, respectively, and Liene Spruzeniece (Geoanalytical Electron Microscopy and Spectroscopy (GEMS) unit) for support with electron microscopy. The APT work was undertaken at the Australian Centre for Microscopy and Microanalysis, University of Sydney, and we are grateful to Takanori Sato for technical assistance. Contributor roles: MRL and LD obtained the funding; MRL and CJF undertook the scanning electron microscopy, LD and SG transmission Kikuchi diffraction, MRL transmission electron microscopy, and LD, JG, and LT atom probe tomography; MRL wrote the original draft, and all authors contributed to review and editing. This research was funded by the UK Science and Technology Facilities Council through grants ST/T002328/1, ST/W001128/1, and ST/T506096/1. For the purpose of open access, the author(s) has applied a Creative Commons Attribution (CC BY) license to any Author Accepted Manuscript version arising from this submission.

Data availability statement—The data that support the findings of this study are available in the supplementary material of this article.

Editorial Handling—Dr. Andrew G. Tomkins

REFERENCES

Alexander, C. M. O'D., Howard, K. T., Bowden, R., and Fogel, M. L. 2013. The Classification of CM and CR Chondrites Using Bulk H, C and N Abundances and

Isotopic Compositions. *Geochimica et Cosmochimica Acta* 123: 244–260.

Bischoff, A., Scott, E. R. D., Metzler, K., and Goodrich, C. A. 2006. Nature and Origins of Meteoritic Breccias. In *Meteorites and the Early Solar System II*, edited by D. S. Lauretta, and H. Y. McSween, Jr., 679–712. Tuscon, AZ: University of Arizona Press.

Cairney, J. M., McCarroll, I., Chen, Y.-S., Eder, K., Sato, T., Liu, Z., Rosenthal, A., and Wepf, R. 2019. Correlative UHV-Cryo Transfer Suite: Connecting Atom Probe, SEM-FIB, Transmission Electron Microscopy Via an Environmentally-Controlled Glovebox. *Microscopy and Microanalysis* 25: 2494–95.

Floyd, C. J., Macante, A., Daly, L., and Lee, M. R. 2023. Unravelling Petrofabrics in the Brecciated CM Chondrite Cold Bokkeveld. *54th Lunar and Planetary Science Conference*, abstract #1477.

Genge, M. J., and Grady, M. M. 1999. The Fusion Crusts of Stony Meteorites: Implications for the Atmospheric Reprocessing of Extraterrestrial Materials. *Meteoritics & Planetary Science* 34: 341–356.

Goswami, J. N., and Lal, D. 1979. Formation of the Parent Bodies of the Carbonaceous Chondrites. *Icarus* 40: 510–521.

Graham, A. L., Bevan, A. W. R., and Hutchison, R. 1985. *Catalogue of Meteorites*, 4th ed. London/Tucson, AZ: London British Museum (Natural History)/University of Arizona Press. 460.

Greenwood, R. C., Lee, M. R., Hutchison, R., and Barber, D. J. 1994. Formation and Alteration of CAIs in Cold Bokkeveld (CM2). *Geochimica et Cosmochimica Acta* 58: 1913–35.

Hanna, R. D., Ketcham, R. A., Zolensky, M., and Behr, W. 2015. Impact-Induced Brittle Deformation, Porosity Loss, and Aqueous Alteration in the Murchison CM Chondrite. *Geochimica et Cosmochimica Acta* 171: 256–282.

Haughton, D. R., Roeder, P. L., and Skinner, B. J. 1974. Solubility of Sulfur in Mafic Magmas. *Economic Geology* 69: 451–467.

Howard, K. T., Alexander, C. M. O'D., Schrader, D. L., and Dyl, K. A. 2015. Classification of Hydrous Meteorites (CR, CM and C2 Ungrouped) by Phyllosilicate Fraction: PSD-XRD Modal Mineralogy and Planetesimal Environments. *Geochimica et Cosmochimica Acta* 149: 206–222.

Krietsch, D., Busemann, H., Riebe, M. E. I., King, A. J., Alexander, C. M. O'D., and Maden, C. 2021. Noble Gases in CM Carbonaceous Chondrites: Effect of Parent Body Aqueous and Thermal Alteration and Cosmic Ray Exposure Ages. *Geochimica et Cosmochimica Acta* 310: 240–280.

Langbroek, M., Jenniskens, P., Kriegsman, L. M., Nieuwenhuis, H., De Kort, N., Kuiper, J., Van Westrenen, W., et al. 2019. The CM Carbonaceous Chondrite Regolith Diepenveen. *Meteoritics & Planetary Science* 54: 1431–61.

Lauretta, D. S., Hergenrother, C. W., Chesley, S. R., Leonard, J. M., Pelgrift, J. Y., Adam, C. D., Al Asad, M., et al. 2019. Episodes of Particle Ejection from the Surface of the Active Asteroid (101955) Bennu. *Science* 366: eaay544.

Lentfort, S., Bischoff, A., Ebert, S., and Patzek, M. 2021. Classification of CM Chondrite Breccias—Implications for the Evaluation of Samples from the OSIRIS-REx and Hayabusa2 Missions. *Meteoritics & Planetary Science* 56: 127–147.

Lindgren, P., Hanna, R. D., Dobson, K. J., Tomkinson, T., and Lee, M. R. 2015. The Paradox between Low Shock-Stage and Evidence for Compaction in CM Carbonaceous Chondrites Explained by Multiple Low-Intensity Impacts. *Geochimica et Cosmochimica Acta* 148: 159–178.

Lindgren, P., Lee, M. R., Sofe, M. R., and Zolensky, M. E. 2013. Clasts in the CM2 Carbonaceous Chondrite Lonewolf Nunataks 94101: Evidence for Aqueous Alteration Prior to Complex Mixing. *Meteoritics & Planetary Science* 48: 1074–90.

Lodders, K. 2003. Solar System Abundances and Condensation Temperatures of the Elements. *The Astrophysical Journal* 591: 1220–47.

Lodders, K. 2021. Relative Atomic Solar System Abundances, Mass Fractions, and Atomic Masses of the Elements and their Isotopes, Composition of the Solar Photosphere, and Compositions of the Major Chondritic Meteorite Groups. *Space Science Reviews* 217: 44.

Lunning, N. G., Corrigan, C. M., McSween, H. Y., Jr., Tenner, T. J., Kita, N. T., and Bodnar, R. J. 2016. CV and CM Chondrite Impact Melts. *Geochimica et Cosmochimica Acta* 189: 338–358.

Matsumoto, T., Noguchi, T., Miyake, A., Igami, Y., Haruta, M., Seto, Y., Miyaharaet, M., et al. 2024. Influx of Nitrogen-rich Material from the Outer Solar System Indicated by Iron Nitride in Ryugu Samples. *Nature Astronomy* 8: 207–215.

Matsuoka, M., Nakamura, T., Hiroi, T., Okumura, S., and Sasaki, S. 2020. Space Weathering Simulation with Low-Energy Laser Irradiation of Murchison CM Chondrite for Reproducing Micrometeoroid Bombardments on C-Type Asteroids. *The Astrophysical Journal Letters* 890: L23.

Matsuoka, M., Nakamura, T., Kimura, Y., Hiroi, T., Nakamura, R., Okumura, S., and Sasaki, S. 2015. Pulse-Laser Irradiation Experiments of Murchison CM2 Chondrite for Reproducing Space Weathering on C-Type Asteroids. *Icarus* 254: 135–143.

Metzler, K. 2004. Formation of Accretionary Dust Mantles in the Solar Nebula: Evidence from Preirradiated Olivines in CM Chondrites. *Meteoritics & Planetary Science* 39: 1307–19.

Metzler, K., Bischoff, A., and Stoffler, D. 1992. Accretionary Dust Mantles in CM Chondrites: Evidence for Solar Nebula Processes. *Geochimica et Cosmochimica Acta* 56: 2873–97.

Noguchi, T., Matsumoto, T., Miyake, A., Igami, Y., Haruta, M., Saito, H., Hata, S., et al. 2023. A Dehydrated Space-Weathered Skin Cloaking the Hydrated Interior of Ryugu. *Nature Astronomy* 7: 170–181.

Rubin, A. E. 2012. Collisional Facilitation of Aqueous Alteration of CM and CV Carbonaceous Chondrites. *Geochimica et Cosmochimica Acta* 90: 181–194.

Rubin, A. E., Trigo-Rodriguez, J. M., Huber, H., and Wasson, J. T. 2007. Progressive Aqueous Alteration of CM Carbonaceous Chondrites. *Geochimica et Cosmochimica Acta* 71: 2361–82.

Scott, E. R. D., Keil, K., and Stöffler, D. 1992. Shock Metamorphism of Carbonaceous Chondrites. *Geochimica et Cosmochimica Acta* 56: 4281–93.

Suttle, M. D., Genge, M. J., and Russell, S. S. 2017. Shock Fabrics in Fine-Grained Micrometeorites. *Meteoritics & Planetary Science* 52: 2258–74.

Thompson, M. S., Loeffler, M. J., Morris, R. V., Keller, L. P., and Christoffersen, R. 2019. Spectral and Chemical Effects of Simulated Space Weathering of the Murchison CM2 Carbonaceous Chondrite. *Icarus* 319: 499–511.

Tomeoka, K., Kiriyama, K., Nakamura, K., Yamahana, Y., and Sekine, T. 2003. Explosive Dispersal of Hydrated Asteroids by Impact as a Mechanism to Produce Interplanetary Dust. *Nature* 423: 60–62.

Tomeoka, K., Yamahana, Y., and Sekine, T. 1999. Experimental Shock Metamorphism of the Murchison CM Carbonaceous Chondrite. *Geochimica et Cosmochimica Acta* 63: 3683–3703.

Tomioka, N., Yamaguchi, A., Ito, M., Uesugi, M., Imae, N., Shirai, N., Ohigashi, T., et al. 2023. A History of Mild Shocks Experienced by the Regolith Particles on Hydrated Asteroid Ryugu. *Nature Astronomy* 7: 669–677.

Tyburczy, J. A., Frisch, B., and Ahrens, T. J. 1986. Shock-Induced Volatile Loss from a Carbonaceous Chondrite: Implications for Planetary Accretion. *Earth and Planetary Science Letters* 80: 201–7.

Vacher, L., Marrocchi, Y., Villeneuve, J., Verdier-Paoletti, M., and Gounelle, M. 2018. Collisional and Alteration History of the CM Parent Body. *Geochimica et Cosmochimica Acta* 239: 213–234.

Wilson, L., Keil, K., Browning, L. B., Krot, A. N., and Bourcier, W. 1999. Early Aqueous Alteration, Explosive Disruption, and re-Processing of Asteroids. *Meteoritics & Planetary Science* 34: 541–557.

Yang, X., Hanna, R. D., Davis, A. M., Neander, A. I., and Heck, P. R. 2022. A Record of Post-Accretion Asteroid Surface Mixing Preserved in the Aguas Zarcas Meteorite. *Nature Astronomy* 6: 1051–58.

Yang, X.-M. 2012. Sulphur Solubility in Felsic Magmas: Implications for Genesis of Intrusion-Related Gold Mineralization. *Geoscience Canada* 39: 17–32.

Zolensky, M. E., Abreu, N. M., Velbel, M. A., Rubin, A., Chaumard, N. l., Noguchi, T., and Michikami, T. 2018. Chapter 2—Physical, Chemical, and Petrological Characteristics of Chondritic Materials and their Relationships to Small Solar System Bodies. In *Primitive Meteorites and Asteroids*, edited by N. Abreu. Amsterdam: Elsevier.

Zolensky, M. E., Mittlefehldt, D. W., Lipschutz, M. E., Wang, M.-S., Clayton, R. N., Mayeda, T. K., Grady, M. N., Pillinger, C., and Barber, D. 1997. CM Chondrites Exhibit the Complete Petrologic Range from Type 2 to 1. *Geochimica et Cosmochimica Acta* 61: 5099–5115.

Zolensky, M., Mikouchi, T., Hagiy, K., Ohsumi, K., Komatsu, M., Cheng, A., and Le, L. 2022. Evidence for Impact Shock and Regolith Transportation on CM, CI, and CV Chondrite Parent Asteroids. *Meteoritics & Planetary Science* 57: 1902–19.

SUPPORTING INFORMATION

Additional supporting information may be found in the online version of this article.

Figure S1. BSE image and corresponding EDS element maps of the bead and shards. In the BSE image, the vesicles are black, and small white grains are Fe-Ni sulfide. The bead and shards have an Mg-Fe silicate composition, with element abundances similar to the enclosing fine-grained clastic matrix.

Figure S2. APT mass spectra for tips M14 (upper) and M22 (lower).

Table S1. Elemental compositions of CM chondrite melts normalized to bulk CM carbonaceous chondrite (data from Lodders, 2021) and Si.